Check for updates

Atomic mechanism of metal crystal nucleus formation in a single-walled carbon nanotube

Kecheng Cao[1], Johannes Biskupek [1], Craig T. Stoppiello[2], Robert L. McSweeney[2],
Thomas W. Chamberlain [3], Zheng Liu [4,5], Kazu Suenaga[4], Stephen T. Skowron [2], Elena Besley [2],
Andrei N. Khlobystov [2 ✉] and Ute Kaiser [1 ✉]

Knowing how crystals nucleate at the atomic scale is crucial for understanding, and in turn controlling, the structure and properties of a wide variety of materials. However, because of the scale and highly dynamic nature of nuclei, the formation and early growth of nuclei are very difficult to observe. Here, we have employed single-walled carbon nanotubes as test tubes, and an 'atomic injector' coupled with aberration-corrected transmission electron microscopy, to enable in situ imaging of the initial steps of nucleation at the atomic scale. With three different metals we observed three main processes prior to heterogeneous nucleation: formation of crystal nuclei directly from an atomic seed (Fe), from a pre-existing amorphous nanocluster (Au) or by coalescence of two separate amorphous sub-nanometre clusters (Re). We demonstrate the roles of the amorphous precursors and the existence of an energy barrier before nuclei formation. In all three cases, crystal nucleus formation occurred through a two-step nucleation mechanism.

Nucleation lies at the heart of the crystallization process and critically determines the structure and size distribution of crystals and thus the functional properties of all materials, from semiconductors to pharmaceuticals[1]. Classical nucleation theory (CNT), developed to elucidate the nucleation of crystals, describes crystal formation in a single step from monomers (atom, ion or molecule), by attachment of individual monomers to an ordered structure, overcoming a single free-energy barrier[2,3]. This can be extended to rationalize the formation and nucleation of crystals through thermodynamically metastable precursors (ordered or disordered) in a single step[3,4]. However, there are a number of experimental observations that cannot be satisfactorily explained using this theory, leading to the postulation of the more complicated and contentious two-step nucleation mechanism (TSNM)[5–10]. This assembly pathway involves the initial formation of an amorphous 'precursor' phase, which is subsequently superseded by a more stable crystalline phase[11–14], or formation of stable species (ordered or disordered), which never dissociate even in undersaturated conditions and can crystallize if more monomer is supplied[15–18]. As a result of the two energy barriers in a TSNM, the initially formed stable or metastable precursor phase can either proceed to crystallize into a crystalline phase by overcoming an additional energy barrier for crystallization or dissociate back into monomers by overcoming the energy barrier for monomer detachment[3].

A range of analytical techniques, such as X-ray diffraction[19,20], atomic force microscopy[3,21,22] and optical microscopy[23], are commonly applied to investigate and establish different mechanisms of nucleation processes. For example, cryogenic transmission electron microscopy (cryo-TEM) allows imaging of the different nucleation stages of inorganic and organic compounds, such as magnetite[15] or dyes in solution[24], which are frozen and suspended

so that the nucleation processes are measured in ex situ discrete steps. An alternative liquid-cell TEM technology enables imaging of the nucleation and growth processes of metal nanocrystals (such as Au[11] and Pt[25]) and inorganic compounds (such as PbS[26]) in solutions in real time with high temporal and spatial resolution. However, both the sheer volume of the liquid and the material of the liquid-cell window inevitably scatter electrons during the TEM imaging process, which, combined with the lack of control over the location and rate of seed nucleation and the ephemeral nature of the nucleation process, preclude the observation of the very early stages of nucleation with atomic resolution. Essentially, an atomically accurate description of the nucleation process is currently hindered by the fact that the critical nucleus sizes are believed to fall in the range of 100–1,000 atoms, which is inaccessible for atomically resolved investigations by any current analytical methods. Therefore, a conceptually new experimental approach is necessary to enable the direct observation of nucleation at the atomic level in real time, and to allow observation to be conducted in a controlled and well-defined environment[27]. Here we apply in situ low-voltage aberration-corrected high-resolution TEM (AC-HRTEM) to study the nucleation of a metal crystal nucleus at the single atom level inside an electron-transparent test tube, a single-walled carbon nanotube (SWNT), which possesses a well-defined atomically smooth surface and outstanding thermal, mechanical and chemical stability under a range of conditions, including an 80-keV electron beam[28–31].

Results and discussion

Fe crystal nuclei formed from an atomic seed. In previous works, we have demonstrated that SWNTs can act as effective host structures for extremely small (30–60 atoms) metal clusters[29,31]. In this
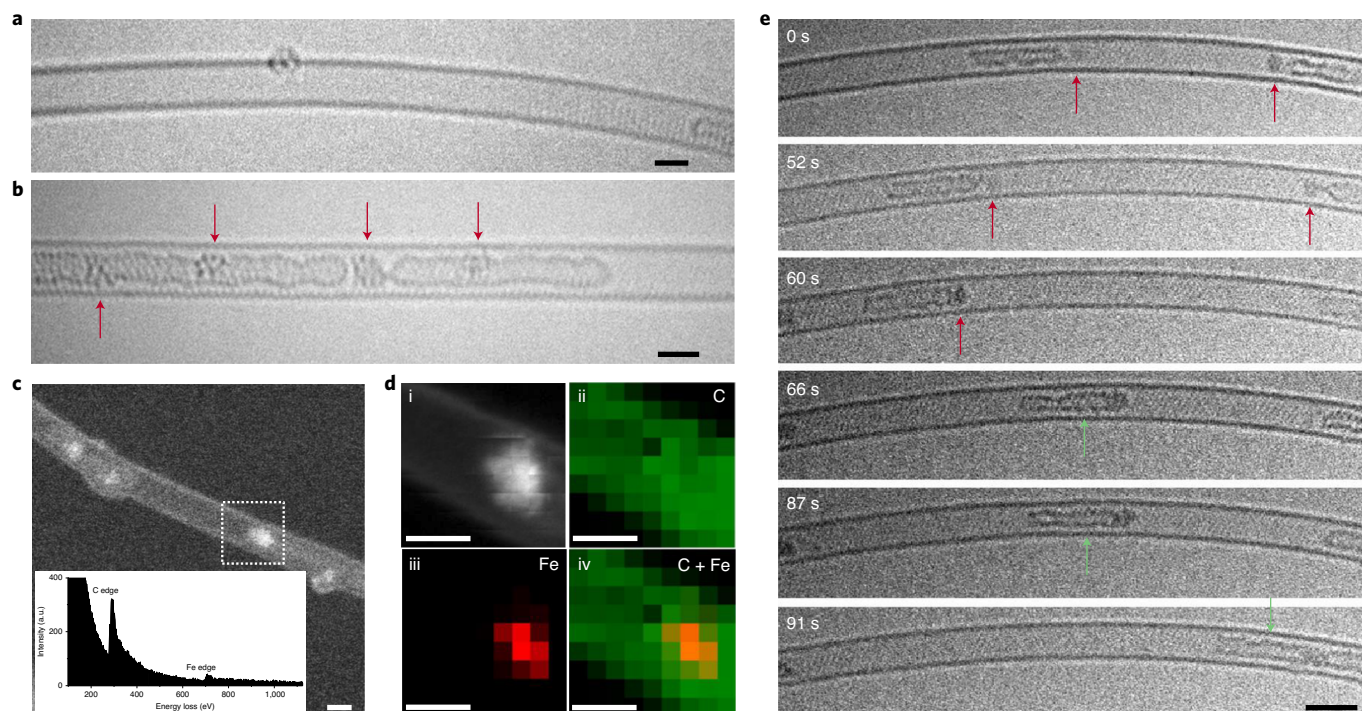
Fig. 1 | Structure of Fe@SWNT and time-series AC-HRTEM images of an atomic injector. a, AC-HRTEM image showing a SWNT with three Fe atoms on its wall. Scale bar, 1 nm. **b**, A SWNT containing Fe clusters and amorphous carbon combined in a variety of different structures (Fe clusters are indicated by the red arrows). The first, second and fourth Fe clusters from left to right combine with amorphous carbon while the third is an isolated Fe cluster. Scale bar, 1 nm. **c**, HAADF-STEM image of Fe@SWNT with an EELS spectrum (inset) recorded in the white boxed area. Scale bar, 1 nm. **d**, EELS mapping of the selected area in **c**: (i) HAADF-STEM image of the selected area; (ii) distribution of carbon; (iii) distribution of iron; (iv) distribution of carbon and iron. Scale bars, 1 nm. **e**, A typical example of an Fe@SWNT-based atomic injector as a time series of AC-HRTEM images, with an Fe cluster translating back and forth from 0 s to 60 s and an Fe cluster–amorphous carbon complex translating from the left side to the right from 60 s to 91 s under 80-keV electron-beam irradiation. The positions of the Fe cluster are indicated by red arrows and the positions of the Fe cluster–amorphous carbon complex by green arrows. Scale bar, 2 nm. More detailed information about this process is provided in Supplementary Fig. 2.

study, we extend this approach to atomic-scale experiments that allow the observation of the initial steps of the nucleation processes of γ-Fe, Au and Re crystal nuclei, at the atomic level and in real time, by means of low-voltage AC-HRTEM imaging. The SWNT provides an ideal cavity for atom transport and a substrate for the heterogeneous nucleation of metal, which prevents ionization by the electron beam due to its conductive structure. Here, the electron beam of the TEM is not only an imaging probe but also a stimulus for the nucleation processes by transferring kinetic energy from the incident electrons to the atoms. The transferred kinetic energy has a maximum value and computable distribution (Supplementary Fig. 1), and it is able to drive the chemical reactions of molecules[28] and the dynamics of metal clusters[29]. In the case of metal clusters, the transferred kinetic energy increases their total free energy in a fashion similar to a heating process. Here, the increase in total free energy can be controlled by adjusting the accelerating voltage and dose rate of the electron beam, thus promoting the nucleation processes of metal crystallites in a similar fashion to a thermal activation. To investigate nucleation from the most initial stages with atomic resolution, it is important to obtain a fixed and observable nucleation seed with only a few atoms. As shown in Fig. 1a, a cluster containing three Fe atoms located on the wall of a SWNT can serve as a nucleation seed in the present experiments. During nucleation in bulk, the additional atoms or molecules are delivered to the seed by random collisions, which is a thermally driven stochastic process with complex mechanisms. In a SWNT the situation is significantly simplified: while the wall of the nanotube provides a substrate for nucleation, mobile clusters of amorphous carbon liberated from

ferrocene serve as vehicles for the delivery of Fe atoms to the growing nucleus, atom by atom, effectively acting as an 'atomic injector'.

Amorphous carbon forms a complex with the Fe atoms (Fig. 1b, Fe atoms are indicated by the rightmost red arrow), which appears to be very mobile, sliding along the nanotube cavity on the timescale of a few seconds, probably driven by thermal energy or electron-beam excitation, due to the extremely low friction of the atomically smooth SWNT[32–34] (Supplementary Section 3). High-angle annular dark-field scanning TEM (HAADF-STEM) and corresponding electron energy loss spectroscopy (EELS) mapping (Fig. 1c,d) confirm the presence of Fe in the highly mobile atomic injector. The time-series AC-HRTEM images in Fig. 1e show a typical example of the atomic injector in action (Supplementary Section 3): stimulated by the electron beam, a cluster of Fe atoms move back and forth during the first 60 s. Owing to the fact the Fe cluster is moving quickly and stops at two positions in the SWNT during the exposure time of 1 s per frame, two images with lower contrast (indicating partial occupancy) appear in frames at 0 s and 52 s. At 60 s, the carbon cluster bonds to the Fe cluster and then translates to the right side of the SWNT in the next 25 s.

The entire nucleation process of γ-Fe is successfully observed and recorded by AC-HRTEM using 80-keV electrons with a dose rate of 1.4×10^6 e$^-$ nm^{-2} s^{-1}, providing a steady source of energy to the atoms, with the SWNT wall acting as substrate for a nucleation seed (Supplementary Video 1). The first stage (0–13 s, Fig. 2) shows the formation of a 'diatomic seed': two Fe atoms form a pair on the outside of the SWNT wall with a distance of 0.32–0.34 nm between the metal atoms. This distance is substantially longer than the
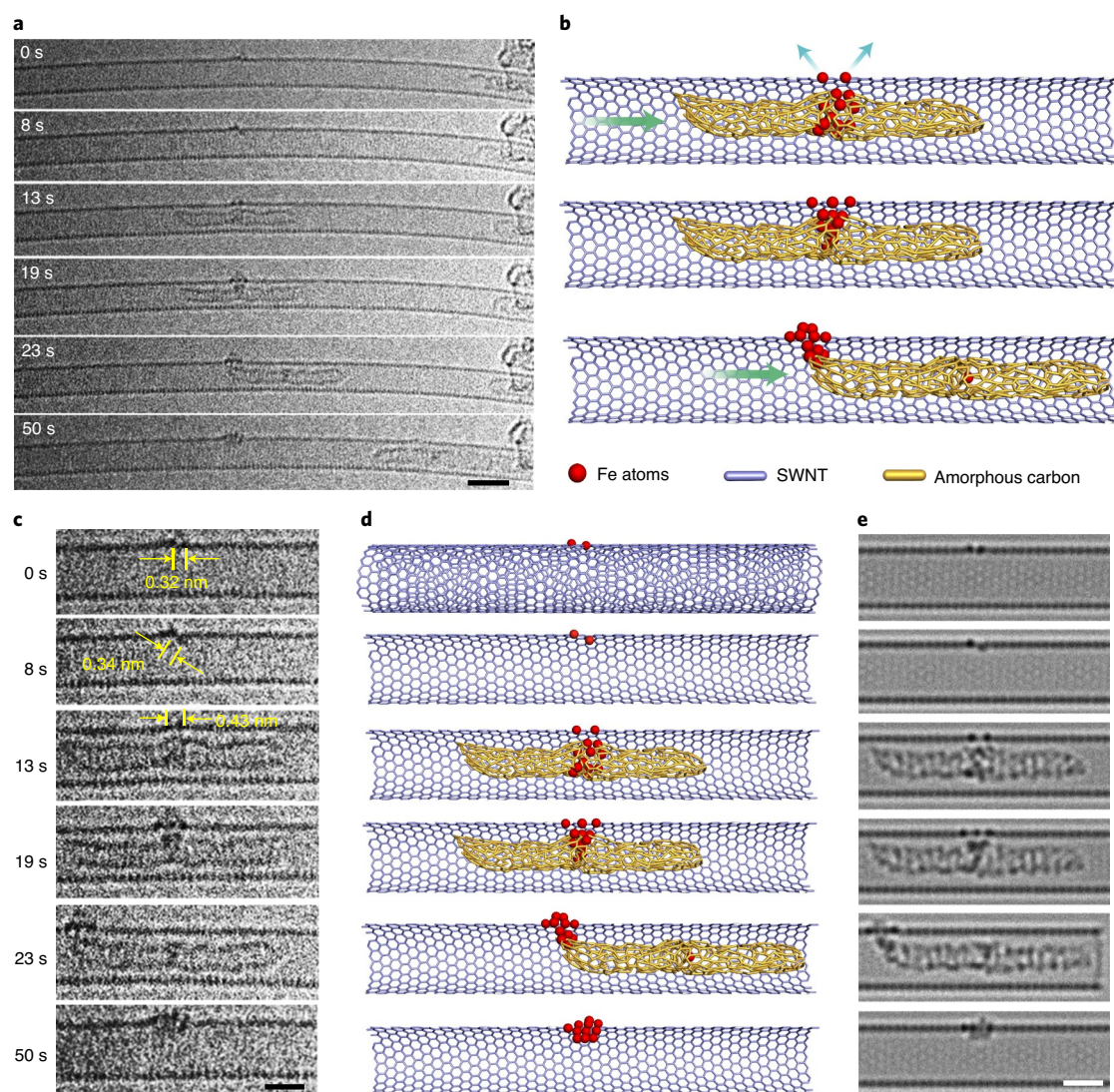
Fig. 2 | Sequential AC-HRTEM images and corresponding simulations showing the first and second stages of γ-Fe crystallite nucleation. a, AC-HRTEM raw images of the first stage from 0 s to 13 s, 'diatomic seed' formation, and the second stage from 13 s to 50 s, the 'atom delivery process'. Exposure time, 0.25 s per frame. Scale bar, 2 nm. **b**, Schematic showing the role of the atomic injector, in which the atomic injector is propelled to the seed, providing individual Fe atoms, before it continues moving along the SWNT cavity (the blue arrows indicate the steric hindrance between the diatomic seed and the atomic injector and the green arrows indicate the direction in which the atomic injector moves). **c**, Enlarged regions of the AC-HRTEM series are shown in **a**, with atomic separations shown. The fifth rows in **c** and **e** are shifted to enable a full view of the atomic injector. The distances between two Fe atoms in the first three frames are labelled in yellow. Scale bar, 1 nm. **d**, Modelled structures corresponding to the experimental images in **c**. The chiral index of the SWNT is $n = 18$, $m = 2$, as calculated in Supplementary Fig. 14. **e**, Simulated TEM images from the structures in **d**. The SWNTs in the modelled structures in **b** and **d** have clipping planes to highlight the structure of Fe clusters. Scale bar, 1 nm.

calculated equilibrium bond length of 0.20 nm for an isolated Fe_2 molecule (Supplementary Section 1), and corresponds to a reduction in the bond energy of the dimer from 2.2 eV (at 0.20 nm) to 0.8 eV (at 0.33 nm). This demonstrates the templating role of the underlying SWNT substrate in controlling the Fe–Fe distance and making it more comparable to bulk γ-Fe (0.29 nm) than gas-phase Fe_2. At 8 s, the right Fe atom passes through the carbon wall and enters into the cavity of the SWNT (Fig. 2c). Given that it is not possible for atoms to permeate the carbon lattice of a SWNT, the observed migration of Fe indicates the presence of vacancy defects in the SWNT wall, which may facilitate bonding of the Fe atoms to the SWNT. At 13 s, the atomic injector translates along the nanotube and moves toward the diatomic seed (Fig. 2a). The consequence of the interaction between the mobile atomic injector and the stationary seed becomes apparent in the next sequence of events (13–50 s,

Fig. 2b,c) in which the right Fe atom of the seed is pushed out and the distance between the two Fe atoms is increased to 0.43 nm. The enlarged inter-atomic distance corresponds to a reduction in the bond energy of an isolated dimer by 90% to only 0.2 eV, and as such is more akin to two independent Fe atoms held apart by bonding to the SWNT than an Fe_2 dimer.

The separation frees up space for a third atom, which subsequently migrates from the atomic injector into the seed at 19 s, signifying the beginning of the second stage of nucleation—the 'atom delivery' process (13–50 s). Over the next 4 s, the diatomic seed grows into a cluster of 17 Fe atoms (determined from image analysis in Supplementary Section 7), with only one Fe atom remaining in the atomic injector. The structure of the growing Fe cluster at this stage stays amorphous. Metallic bonding may act as an attractive force, pulling the atomic injector towards the Fe seed and holding
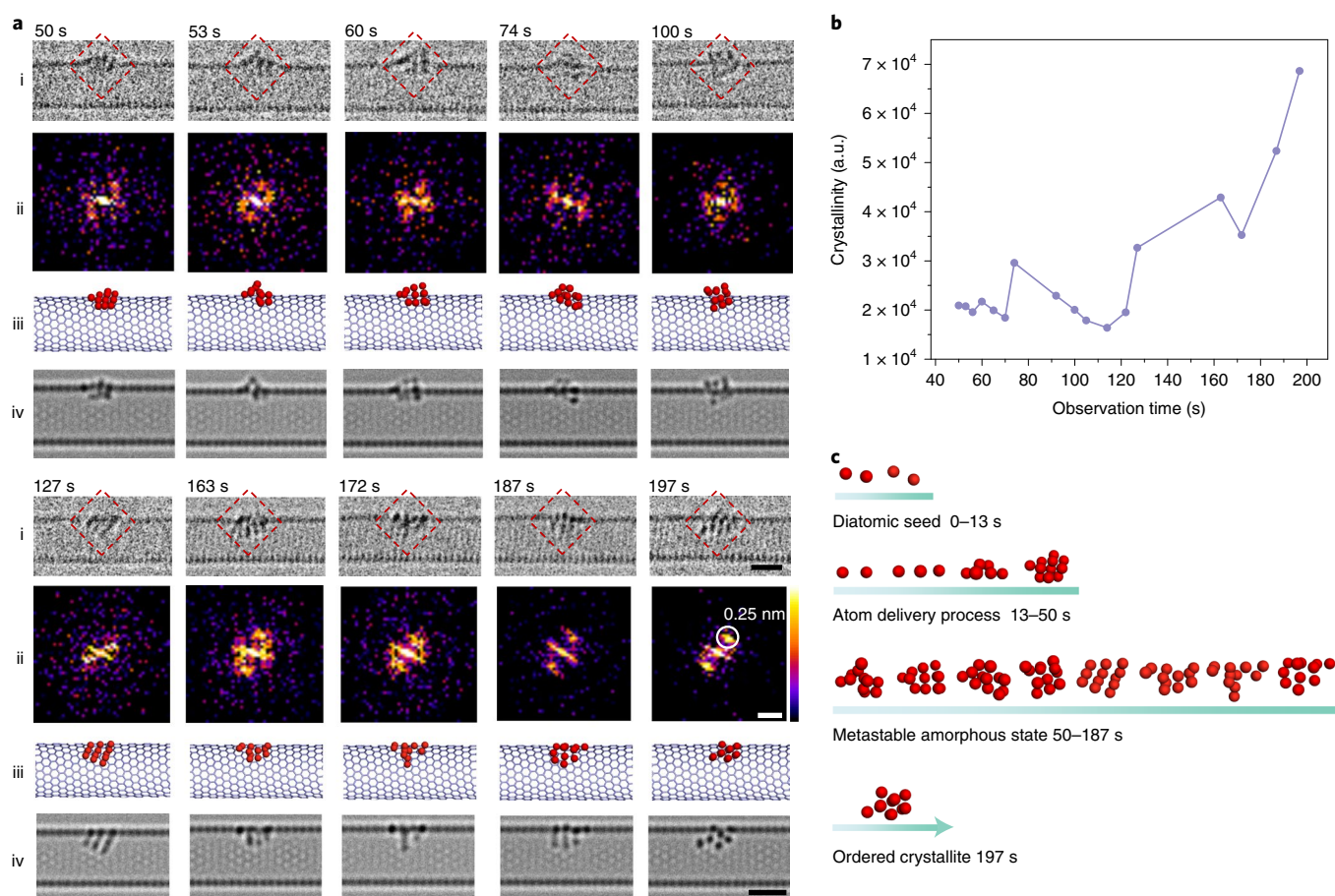
Fig. 3 | Sequential AC-HRTEM images and corresponding image simulations showing the third and fourth stages of γ-Fe crystallite nucleation.
a, Time-series AC-HRTEM images of the third 'metastable amorphous state' stage from 50 s to 187 s and the fourth 'ordered crystallite' stage at 197 s are shown in the first row (i). Scale bar, 1 nm. The exposure time for the frames between 50 and 127 s is 0.5 s, and 1.0 s from 127 s to 197 s. The FFT results corresponding to the outlined areas in the AC-HRTEM images are depicted in the second row (ii) and used to quantify the crystallinity of the Fe cluster at each point in time (via the appearance of an extra Fe reflection, Supplementary Section 6). Scale bar, 5 nm⁻¹. The modelled structures and simulated TEM images for the proposed structures of the Fe clusters that correspond to the AC-HRTEM images in the same column are presented in the third (iii) and fourth rows (iv). Scale bar, 1 nm. **b**, Quantified measure of the crystallinity by comparing the intensities of the reflection spots in the FFT results for the Fe clusters. The measured reflection spots are chosen from the probable characteristic diffraction spot areas where the γ-Fe-reflection appears. **c**, Timeline of the whole experiment, with the structural evolution of the γ-Fe crystallite consisting of the four stages of crystallite formation.

it in place during the atom delivery stage, because after most of the Fe atoms are injected (at 23 s, Fig. 2a) the remaining, relatively weak van der Waals force is unable to retain the mobile atomic injector in the vicinity of the Fe cluster and the atomic injector moves away along the nanotube (50 s in Fig. 2a). The real-time imaging of the atom delivery process enables the visualization of precise details of the initial stages of crystallite nucleation, showing how the discrete atoms become a cluster by joining to the diatomic seed in steps.

At the point of atomic injector departure (50 s), a 'metastable amorphous state' stage begins as the structureless sub-nanometre cluster containing ~17 Fe atoms undergoes continuous reorganization for the next 147 s. During this stage, the Fe atoms shuttle back and forth between the outer and inner surface of the SWNT, with the inter-atomic distances and coordination numbers of Fe atoms continuously and randomly changing over time (Fig. 3a). The highly dynamic nature of the metal cluster at this stage is consistent with the notion of a metastable amorphous cluster, such that the positions of the constituent atoms are extremely sensitive to local conditions such as temperature, pressure and the local environment, all of which can influence the reorganization process and thus the final structure of the crystallite nucleus. Finally, the amorphous cluster becomes ordered (at 197 s, Fig. 3a) with the Fe atoms adopting

uniform inter-atomic distances matching the (111) plane of the γ-Fe crystal lattice. This represents the fourth stage, designated the 'ordered crystallite' stage, which marks the end of the nucleation process, as from this point further growth of the crystallite will be strictly templated by the structure of the ordered crystal-like nucleus. The degree of atomic order in the Fe cluster was elucidated by fast Fourier transform (FFT) analysis (second row, Fig. 3a), allowing quantitative analysis of changes in the relative degree of crystallinity over time (Fig. 3b and Supplementary Section 6).

In the diatomic seed stage, interactions between the Fe diatomic seed and the SWNT reduce the total free energy of the dimer and stabilize the seed, which is similar to the stabilization that occurs in heterogeneous nucleation processes where the nucleation happens at the gas–solid, gas–liquid or solid–liquid interface. However, the diatomic seed is able to dissociate back into discrete atoms (Supplementary Fig. 8), highlighting the metastable nature of the seed and that the free-energy barrier to Fe-atom detachment is small for seeds of this size under the present conditions (room temperature, vacuum, carbon surface) (Supplementary Section 4). Calculations (Supplementary Section 1) show that the atomization energy required for Fe_2 is 2.2 eV (1.1 eV per atom), rising to 4.3 eV (1.4 eV per atom) for Fe_3. The observed extended lifetime of the
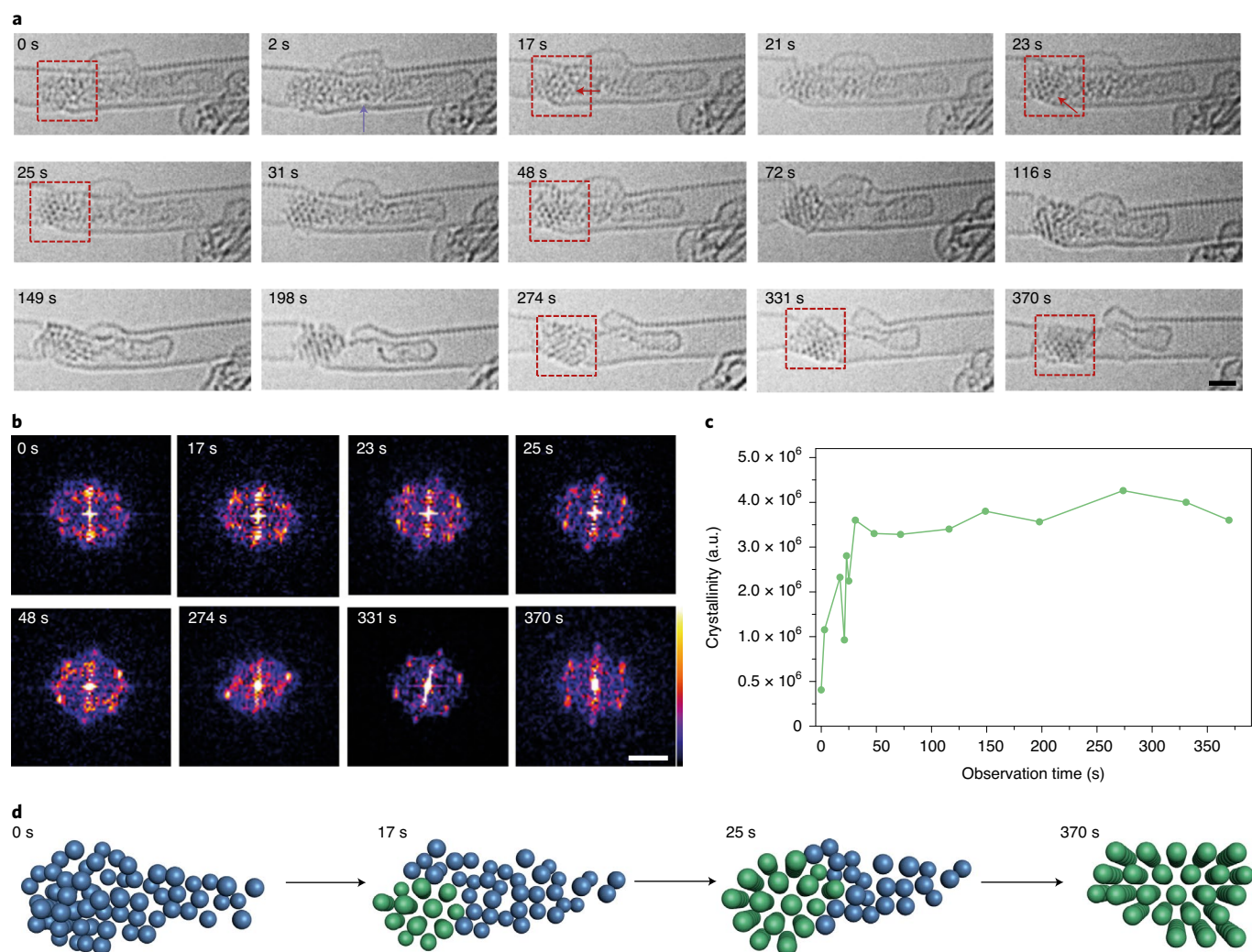
Fig. 4 | Electron-beam-stimulated nucleation of Au crystallite from the amorphous state. a, Time-series AC-HRTEM images showing an amorphous Au cluster gradually transforming into its crystalline structure under 80-keV electron-beam irradiation. The formed crystallite is indicated by red arrows. Scale bar, 1 nm. **b**, FFT patterns of the corresponding areas framed by red dotted boxes in **a** demonstrating formation of the Au crystallite. Some Au atoms in this Au cluster diffuse into the neighbouring carbon nanostructure, as indicated by the violet arrow in **a**. Scale bar, 5 nm⁻¹. **c**, Quantified crystallinity of the Au cluster during the nucleation in **a** and **b**. **d**, Schematic of the gradual nucleation of the Au crystallite (the amorphous parts are shown in blue and the crystalline parts in green).

amorphous cluster of Fe atoms indicates its stability when the number of atoms is above 10, as confirmed by the observation that clusters containing ~10 Fe atoms never crystallize or dissociate back to individual atoms (Supplementary Figs. 9 and 10). Significantly, once the growth of the Fe cluster is completed, the Fe cluster containing 17 atoms stays amorphous for over 142 s before crystallizing, which we regard as evidence that a metastable amorphous precursor cluster is necessary for the nucleation of γ-Fe. Under the present experimental conditions, we also observe several examples of stable crystallites of larger sizes, such as a γ-Fe crystallite with ~100 atoms (Supplementary Fig. 10). Overall, these observations are consistent with the existence of two free-energy barriers and an amorphous precursor state during the heterogeneous nucleation of γ-Fe, which is consistent with the pathway proceeding via a TSNM. Although more than 10 Fe atoms appear to be necessary and 17 Fe atoms appear to be sufficient to produce an ordered crystalline nucleus, it must be noted that the critical number of atoms may be different under conditions that differ from those in our experiments, as electron-beam irradiation has previously been shown to affect the nucleation process[11,25]. Being continuously irradiated by the electron

beam, the γ-Fe crystallite begins to interact with the host SWNT, leading to removal of carbon atoms from the SWNT, propagating the growth of a vacancy defect, which finally leads to the rupture of the SWNT after 170 s (Supplementary Section 8)[29].

Au crystal nuclei formed from an amorphous nanocluster. The importance of initially forming a metastable amorphous precursor is further illustrated by nucleation of Au crystallites (Fig. 4). At the start of the experiment, an initial stable amorphous Au cluster can be observed confined in the SWNT. Some Au atoms diffuse into the adjacent carbon nanostructure (violet arrow, Fig. 4a). In the first 16 s of electron-beam irradiation, the atomic structure of the cluster is extremely dynamic and appears amorphous (Supplementary Video 2). At 17 s, a metastable crystallite with a diameter of less than 1 nm can be observed in the Au cluster (red arrow, Fig. 4a), which is confirmed by analysis of the corresponding FFT pattern (Fig. 4b). This tiny crystallite dissociates in the following 5 s and reappears again at 23 s. When the diameter of the crystallite reaches ~1 nm, it becomes stable over extended periods of time, with a well-ordered structure of the (111) face of Au observed. From this point, the nucleation
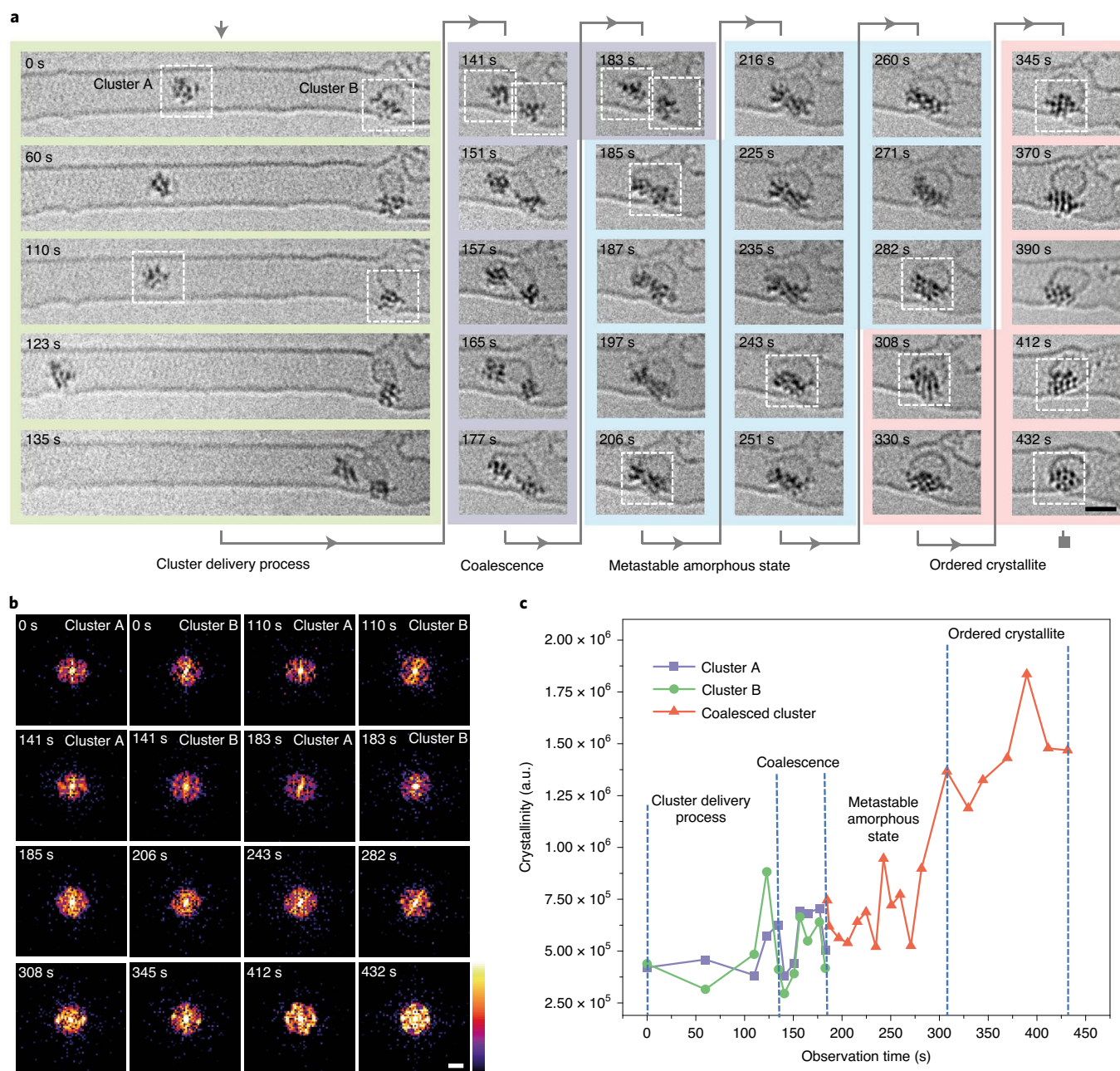
Fig. 5 | Electron-beam-stimulated nucleation of Re crystallite by coalescing two amorphous sub-nanometre Re clusters. a, Time-series AC-HRTEM images showing the four key stages of Re crystallite nucleation, starting with two amorphous sub-nanometre Re clusters (Supplementary Video 3). From 0 s to 135 s, one amorphous cluster located at the left of the SWNT translates and attaches to another amorphous cluster located at the right of the SWNT, which is the first stage of Re nucleation, the 'cluster delivery process'. From 141 s to 183 s, the two clusters contact each other and then coalesce into one amorphous cluster, which is the second stage, 'coalescence'. The coalesced amorphous cluster ceaselessly changes its structure from 185 s to 282 s, in the 'metastable amorphous state' stage. At 308 s, a crystallite is formed and continues restructuring for a further 124 s, in the 'ordered crystallite' stage. Scale bar, 1 nm. **b**, FFT patterns of the corresponding areas framed by white dotted boxes in **a**, analysing the periodic structural information of the Re cluster and crystallite. Scale bar, 5 nm⁻¹. **c**, Quantification of the degree of crystallization for the Re clusters at the different stages depicted in **a**. Cluster A and cluster B are, respectively, the small Re clusters on the left and right sides of the image at the beginning of the experimental image series.

process gradually extends from the tiny crystallite to the whole Au cluster in the following 348 s, reaching a final crystal size that is ~2 nm long and ~1 nm wide at 370 s. The Au crystallite maintains its orientation in the first 28 s of the nucleation process from 23 s to 51 s and subsequently rotates or transforms, displaying different orientations from 51 s to 330 s. During the final stage of nucleation from 331 s to 370 s, the Au crystallite rotates or transforms again to the original (111) face, as can be seen in the FFT patterns of the

areas marked with red frames (Fig. 4a,b). By evaluating the intensity of the spots corresponding to crystalline gold in the FFT patterns, the degree of crystallinity can be estimated (Fig. 4c), showing an abrupt increase of the atomic ordering in the Au cluster during heterogeneous nucleation that demonstrates that crystallization of Au has occurred from an amorphous precursor.

The maximum transferred kinetic energy (E_{T_max}) from the incident 80-keV electrons to the Au atoms is 0.96 eV (Supplementary

Section 2, in which the corresponding differential cross-section as well as the total cross-section of elastic scattering is included). Thus, when being irradiated by the electron beam, the total free energy of the Au cluster increases, allowing it to overcome the energy barrier for transformation from amorphous to crystalline (Supplementary Fig. 5 and Supplementary Section 4). Previous work has demonstrated that energy transferred from the electron beam can influence, melt and even vaporize the different metal nanocrystals[28]. In the case of Au, the metastable amorphous cluster dynamically changes the atomic structure before finally crystallizing under the influence of the electron beam (Fig. 4d). Therefore, we can conclude that the size of the amorphous Au cluster is smaller than the critical size for crystallization under sample preparation conditions but larger than the critical size for crystallization under the TEM observation conditions; that is, only under the influence of electron-beam irradiation has it enough energy to overcome the energy barrier to crystallization. It should be noted that our experiments reveal a discernible Au crystallite with a radius of ~0.45 nm, which is much smaller than the crystal nucleus of 2 nm observed for this metal in the aqueous solution of a liquid TEM cell[11] due to the different conditions for nucleation.

Re crystal nuclei formed by coalescence. Increases in the number of atoms in the cluster help to overcome the free-energy barrier and promote the nucleation process. Therefore, the coalescence of clusters, typically ignored by CNT, can be an important process for nucleation as it enables a rapid increase of the cluster size (Supplementary Section 4). We observe this effect by imaging the coalescence of two stable amorphous Re clusters into a larger amorphous metastable cluster that subsequently crystallizes into a Re crystallite. At the beginning of the TEM time series, two pre-existing sub-nanometre amorphous Re clusters with ~10 atoms each are present in the host SWNT (Fig. 5). The left cluster is mobile, translating along the cavity of the SWNT. The right cluster is fixed on the SWNT by metal–carbon bonding and partly covered by a carbon shell, which can be regarded as the substrate for heterogeneous nucleation. At 135 s, the left cluster translates and attaches to the carbon shell of the right cluster. They come into contact briefly on two occasions via a single Re atom at 151 s and 177 s, and then completely coalesce in 3 s from 183 s to 185 s. The resultant cluster contains ~20 atoms of Re; this appears to be above the critical number allowing the metal to overcome the free-energy barrier for crystallization (Supplementary Fig. 6 and Supplementary Section 4). The process of crystallization starts with the formation of a metastable amorphous state at 185 s, followed by reorganization of Re atoms into a crystallite between 185 and 308 s, which is slightly faster than the nucleation we observe in the case of γ-Fe. At 308 s, the Re crystallite with a recognizable crystalline structure is observed, followed by 124 s of restructuring while maintaining crystallinity, which can be clearly observed as distinguishable lattice planes in the 'ordered crystallite' stage and quantified by FFT (Fig. 5b,c). The overall crystallite formation of Re follows the same TSNM pathway as Au and Fe, with the only difference that the critical size (or number of atoms) required for crystallization is achieved by coalescence of two amorphous Re clusters.

Conclusions

We have imaged the heterogeneous nucleation of three different metals, γ-Fe, Au and Re, in a SWNT, with atomic resolution. All three nucleation processes observed under electron-beam irradiation and at room temperature are consistent with a TSNM framework, proving the validity of this theoretically postulated mechanism[14]. We have directly observed the existence of a metastable amorphous precursor and demonstrated its necessity for the crystallite nucleation processes. The size and number of atoms in the amorphous precursor are critically important for the emergence of a crystallite. In the case of all three metals the critical size is in the sub-2 nm range and the number of atoms necessary for successful crystallization of both γ-Fe and Re lies between 10 and 20. The combined use of a SWNT as the substrate for heterogeneous nucleation and the channel for delivery of metal atoms and the electron beam as a source of energy to simultaneously drive the process and act as an imaging tool sheds light on the formation of a crystal nucleus at the sub-nanometre level—a challenging size range for any other analytical method. These results are particularly important for Fe, Au and Re in the carbon-rich environments present in a variety of industrial contexts, including Fischer–Tropsch catalysis, growth of graphene by chemical vapour deposition or steel manufacturing.

Online content

References

1. Myerson, A. S. & Trout, B. L. Nucleation from solution. *Science* **341**, 855–856 (2013).
2. Kashchiev, D. Thermodynamically consistent description of the work to form a nucleus of any size. *J. Chem. Phys.* **118**, 1837–1851 (2003).
3. Sleutel, M., Lutsko, J., Driessche, A. E. S. V. A. N., Durán-Olivencia, M. A. & Maes, D. Observing classical nucleation theory at work by monitoring phase transitions with molecular precision. *Nat. Commun.* **5**, 5598 (2014).
4. Habraken, W. J. E. M. et al. Ion-association complexes unite classical and non-classical theories for the biomimetic nucleation of calcium phosphate. *Nat. Commun.* **4**, 1507 (2013).
5. Dey, A. et al. The role of prenucleation clusters in surface-induced calcium phosphate crystallization. *Nat. Mater.* **9**, 1010–1014 (2010).
6. Erdemir, D., Lee, A. Y. & Myerson, A. S. Nucleation of crystals from solution: classical and two-step models. *Acc. Chem. Res.* **42**, 621–629 (2009).
7. De, Y. et al. Crystallization by particle attachment in synthetic, biogenic and geologic environments. *Science* **349**, aaa6760 (2015).
8. Gebauer, D. & Cölfen, H. Prenucleation clusters and non-classical nucleation. *Nano Today* **65**, 564–584 (2011).
9. Vekilov, P. G. The two-step mechanism of nucleation of crystals in solution. *Nanoscale* **2**, 2346–2357 (2010).
10. Lutsko, J. F. & Nicolis, G. Theoretical evidence for a dense fluid precursor to crystallization. *Phys. Rev. Lett.* **6**, 0461024 (2006).
11. Loh, N. D. et al. Multistep nucleation of nanocrystals in aqueous solution. *Nat. Chem.* **9**, 77–82 (2017).
12. Nielsen, M. H., Aloni, S. & De Yoreo, J. J. In situ TEM imaging of CaCO₃ nucleation reveals coexistence of direct and indirect pathways. *Science* **345**, 1158–1162 (2014).
13. Gal, A. et al. Calcite crystal growth by a solid-state transformation of stabilized amorphous calcium carbonate nanospheres in a hydrogel. *Angew. Chem. Int. Ed.* **52**, 4867–4870 (2013).
14. Navrotsky, A. Energetic clues to pathways to biomineralization: precursors, clusters and nanoparticles. *Proc. Natl Acad. Sci. USA* **101**, 12096–12101 (2004).
15. Baumgartner, J. et al. Nucleation and growth of magnetite from solution. *Nat. Mater.* **12**, 310–314 (2013).
16. Galkin, O., Chen, K., Nagel, R. L., Hirsch, R. E. & Vekilov, P. G. Liquid–liquid separation in solutions of normal and sickle cell hemoglobin. *Proc. Natl Acad. Sci. USA* **99**, 8479–8483 (2002).
17. Wolf, S. E., Leiterer, J., Kappl, M., Emmerling, F. & Tremel, W. Early homogenous amorphous precursor stages of calcium carbonate and subsequent crystal growth in levitated droplets. *J. Am. Chem. Soc.* **130**, 12342–12347 (2008).
18. Gebauer, D., Völkel, A. & Cölfen, H. Stable prenucleation calcium carbonate clusters. *Science* **322**, 1819–1822 (2008).
19. Sellberg, J. A. et al. Ultrafast X-ray probing of water structure below the homogeneous ice nucleation temperature. *Nature* **510**, 381–384 (2014).
20. Bera, M. K. & Antonio, M. R. Crystallization of Keggin heteropolyanions via a two-step process in aqueous solutions. *J. Am. Chem. Soc.* **138**, 7282–7288 (2016).
21. Yau, S.-T. & Vekilov, P. G. Direct observation of nucleus structure and nucleation pathways in apoferritin crystallization. *J. Am. Chem. Soc.* **123**, 1080–1089 (2001).

22. Lupulescu, A. I. & Rimer, J. D. In situ imaging of silicalite-1 surface growth reveals the mechanism of crystallization. *Science* **344**, 729–732 (2014).
23. Pusey, P. N. & van Megen, W. Phase behaviour of concentrated suspensions of nearly hard colloidal spheres. *Nature* **320**, 340–342 (1986).
24. Tsarfati, Y. et al. Crystallization of organic molecules: nonclassical mechanism revealed by direct imaging. *ACS Cent. Sci.* **4**, 1031–1036 (2018).
25. Zheng, H. et al. Observation of single colloidal platinum nanocrystal growth trajectories. *Science* **324**, 1309–1312 (2009).
26. Evans, J. E., Jungjohann, K. L., Browning, N. D. & Arslan, I. Controlled growth of nanoparticles from solution with in situ liquid transmission electron microscopy. *Nano Lett.* **11**, 2809–2813 (2011).
27. Sosso, G. C. et al. Crystal nucleation in liquids: open questions and future challenges in molecular dynamics simulations. *Chem. Rev.* **116**, 7078–7116 (2016).
28. Skowron, S. T. et al. Chemical reactions of molecules promoted and simultaneously imaged by the electron beam in transmission electron microscopy. *Acc. Chem. Res.* **50**, 1797–1807 (2017).
29. Cao, K. et al. Comparison of atomic scale dynamics for the middle and late transition metal nanocatalysts. *Nat. Commun.* **9**, 3382 (2018).
30. Khlobystov, A. N. Carbon nanotubes: from nano test tube to nano-reactor. *ACS Nano* **5**, 9306–9312 (2011).
31. Zoberbier, T. et al. Interactions and reactions of transition metal clusters with the interior of single-walled carbon nanotubes imaged at the atomic scale. *J. Am. Chem. Soc.* **134**, 3073–3079 (2012).
32. Somada, H., Hirahara, K., Akita, S. & Nakayama, Y. A molecular linear motor consisting of carbon nanotubes. *Nano Lett.* **9**, 62–65 (2009).
33. Warner, J. H. et al. Capturing the motion of molecular nanomaterials encapsulated within carbon nanotubes with ultrahigh temporal resolution. *ACS Nano* **3**, 3037–3044 (2010).
34. Ran, K., Zuo, J. –M., Chen, Q. & Shi, Z. Electron beam stimulated molecular motions. *ACS Nano* **5**, 3367–3372 (2011).

Methods

Materials. Arc-discharge SWNTs were annealed in air to open their termini. The organometallic complexes $Fe(C_5H_5)_2$, $Au(CO)Cl$ and $Re_2(CO)_{10}$ were respectively sealed under vacuum in a quartz ampoule and heated at a temperature slightly above the vaporization point of ferrocene (300 °C), $Au(CO)Cl$ (125 °C) and $Re_2(CO)_{10}$ (150 °C) for three days to ensure complete penetration of the SWNT by the ferrocene, $Au(CO)Cl$ and $Re_2(CO)_{10}$ vapours. The samples were then rapidly cooled to room temperature and the SWNTs washed with tetrahydrofuran (100 ml) to remove any species from the outside of the SWNTs. The samples were then heated at 500 °C for 3 h under argon in a Pyrex tube to remove the ligands.

TEM imaging and simulations. The materials were dispersed in methanol and drop-cast onto lacey carbon-coated copper TEM grids. The time-series AC-HRTEM images in Supplementary Videos 1–3 were obtained on an image-side C_s-corrected FEI Titan 80-300 TEM operated at 80 kV at room temperature. The TEM specimen was heated in air at 150 °C for 5 min shortly before insertion into the TEM column. The HAADF-STEM imaging and corresponding EELS spectrum in Fig. 1 were performed on a JEOL 2100F system with a cold field-emission gun and an aberration DELTA-corrector for the illumination system operated at 60 kV. TEM image simulation was carried out using the multislice program QSTEM. Note that γ-Fe was observed to keep its crystalline structure after it formed during the experiment (197 s to 336 s), but the related images were not acquired because we did not realize the importance of this observation until the cutting process started.

Data availability

All data supporting the findings of this study are available in the manuscript or the Supplementary Information. The data for the electron elastic scattering cross-section that support the findings of this study are publicly available online at https://www.nist.gov/publications/nist-electron-elastic-scattering-cross-section-database-version-40.

Author contributions

R.L.M. prepared the samples. C.T.S. carried out initial analysis of the samples. T.W.C. developed the methodology of filling nanotubes with metal precursors. Z.L., J.B. and K.S. performed the EELS mapping of the sample. K.C. and J.B. investigated of the sample by AC-HRTEM and recorded the videos of nucleation. K.C., J.B., A.N.K. and U.K. discussed the results and analysed the data. E.B. and S.T.S. carried out theoretical modelling. K.C., J.B., A.N.K. and U.K. drafted the manuscript. All the authors have revised the manuscript. U.K. and A.N.K. supervised the research.

Competing interests

The authors declare no competing interests.

Additional information

Supplementary information is available for this paper at https://doi.org/10.1038/s41557-020-0538-9.

Correspondence and requests for materials should be addressed to A.N.K. or U.K.

Reprints and permissions information is available at www.nature.com/reprints.